

The Effect of Sr^{2+} on Luminescence of Ce^{3+} -Doped $(\text{Ca,Sr})_2\text{Al}_2\text{SiO}_7$

Lin, Litian; Shi, Rui; Zhou, Rongfu; Peng, Qi; Liu, Chunmeng; Tao, Ye; Huang, Yan; Dorenbos, Pieter; Liang, Hongbin

DOI

[10.1021/acs.inorgchem.7b01939](https://doi.org/10.1021/acs.inorgchem.7b01939)

Publication date

2017

Document Version

Final published version

Published in

Inorganic Chemistry: including bioinorganic chemistry

Citation (APA)

Lin, L., Shi, R., Zhou, R., Peng, Q., Liu, C., Tao, Y., Huang, Y., Dorenbos, P., & Liang, H. (2017). The Effect of Sr^{2+} on Luminescence of Ce^{3+} -Doped $(\text{Ca,Sr})_2\text{Al}_2\text{SiO}_7$. *Inorganic Chemistry: including bioinorganic chemistry*, 56(20), 12476-12484. <https://doi.org/10.1021/acs.inorgchem.7b01939>

Important note

To cite this publication, please use the final published version (if applicable).
Please check the document version above.

Copyright

Other than for strictly personal use, it is not permitted to download, forward or distribute the text or part of it, without the consent of the author(s) and/or copyright holder(s), unless the work is under an open content license such as Creative Commons.

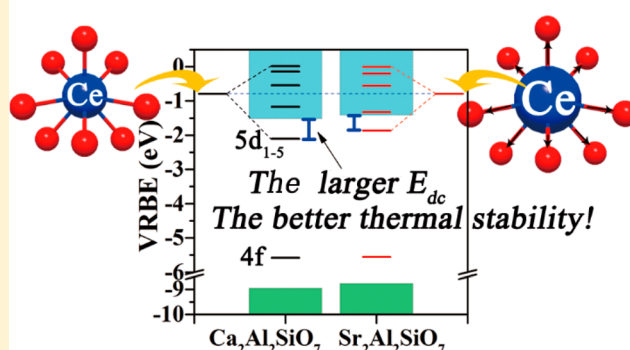
Takedown policy

Please contact us and provide details if you believe this document breaches copyrights.
We will remove access to the work immediately and investigate your claim.

The Effect of Sr²⁺ on Luminescence of Ce³⁺-Doped (Ca,Sr)₂Al₂SiO₇Litian Lin,[†] Rui Shi,[†] Rongfu Zhou,[†] Qi Peng,[†] Chunmeng Liu,[†] Ye Tao,[‡] Yan Huang,[‡] Pieter Dorenbos,[§] and Hongbin Liang^{*,†}[†]MOE Key Laboratory of Bioinorganic and Synthetic Chemistry, KLGHEI of Environment and Energy Chemistry, School of Chemistry, Sun Yat-sen University, Guangzhou 510275, China[‡]Beijing Synchrotron Radiation Facility, Institute of High Energy Physics, Chinese Academy of Sciences, Beijing 100039, China[§]Faculty of Applied Sciences, Delft University of Technology, Mekelweg 15, 2629 JB Delft, The Netherlands

Supporting Information

ABSTRACT: A series of Ce³⁺-doped (Ca,Sr)₂Al₂SiO₇ phosphors with different Ce³⁺ and Ca²⁺/Sr²⁺ concentrations were prepared by a high temperature solid-state reaction technique. To get insight into the structure–luminescence relationship, the impact of incorporation of Sr²⁺ on structure of (Ca,Sr)₂Al₂SiO₇ was first investigated via Rietveld refinement of high quality X-ray diffraction (XRD) data, and then the VUV–UV excitation and UV–vis emission spectra of (Ca,Sr)₂Al₂SiO₇:Ce³⁺ were collected at low temperature. The results reveal that the crystal structure evolution of (Ca,Sr)₂Al₂SiO₇:Ce³⁺ has influences on band gaps and Ce³⁺ luminescence properties including 4f–5d_{*i*} (*i* = 1–5) transition energies, radiative lifetime, emission intensity, quantum efficiency, and thermal stability. Moreover, the influence of Sr²⁺ content on the energy of Eu³⁺–O²⁻ charge-transfer states (CTS) in (Ca,Sr)₂Al₂SiO₇:Eu³⁺ was studied in order to construct vacuum referred binding energy (VRBE) schemes with the aim to further understand the luminescence properties of (Ca,Sr)₂Al₂SiO₇:Ce³⁺. Finally, X-ray excited luminescence (XEL) spectra were measured to evaluate the possibility of (Ca,Sr)₂Al₂SiO₇:Ce³⁺ as a scintillation material.



1. INTRODUCTION

Ce³⁺-activated luminescent materials have drawn much attention due to their scientific importance and practical applications in scintillators, solid state lighting (SSL), persistent luminescence, solar energy converters, and so on.^{1,2} The applications in all these aspects benefit from the typical parity-allowed 4f–5d transition of Ce³⁺ which is characterized by a large absorption cross section and high radiative emission rate. Particularly, the energy of the Ce³⁺ 4f–5d transition can be changed to satisfy specific demands of applications by choosing a suitable host matrix or by tuning its composition, owing to the high sensitivity of the 5d orbital to the variation of local coordination environment.^{3–7} For example, through precisely controlling the composition of Al³⁺/Ga³⁺ in Y₃(Al_{1–*x*}Ga_{*x*})₅O₁₂:Ce³⁺, the first 5d level (5d₁) of Ce³⁺ can be placed at an appropriate position relative to the conduction band maximum (CBM), which makes this series of materials suitable for SSL (*x* = 0)⁸ or persistent luminescence (*x* = 3)^{9,10} applications. This composition engineering procedure has already become an important method in optimizing and exploring novel Ce³⁺-activated materials.^{11–15} More importantly, the change of relative distance between the Ce³⁺ 5d₁ level and the CBM is expected to further influence the thermal stability of Ce³⁺ luminescence after the structural modification.¹⁶ Indeed, the thermal stability is a crucial issue for

applications of luminescent materials in various areas. Therefore, it is of interest and essential to get a systematic and deep insight into the impacts of the tuning of chemical compositions and structure on the band gap, 5d energies, and thermal stability for the different applications of Ce³⁺-activated materials.

Silicates are important host compounds for luminescence of Ce³⁺. For example, Lu₂SiO₅ crystals doped with Ce³⁺ are a commercial scintillator for positron emission tomography (PET).¹⁷ The isomorphous M₂Al₂SiO₇ (M = Ca, Sr) compounds have the melilite crystal structure.¹⁸ This type of compound contains rigid SiO₄⁴⁻ and AlO₄⁵⁻ tetrahedral anionic groups, and alkaline earth cations M²⁺ can be easily modified with Ca²⁺ or Sr²⁺.¹⁹ These structure features are well-suited for the investigation on the influence of different M²⁺ on the band gap energy. Moreover, the single-site occupation of M²⁺ also facilitates the study of composition-dependent 5d energy and luminescence of Ce³⁺ ions.

In this article, the influence of Ca²⁺/Sr²⁺ concentrations on the crystal structure evolution of (Ca,Sr)₂Al₂SiO₇, the VUV–UV–vis photoluminescence, and the X-ray radioluminescence of a series of Ce³⁺-doped (Ca,Sr)₂Al₂SiO₇ were investigated

Received: August 1, 2017

Published: September 27, 2017

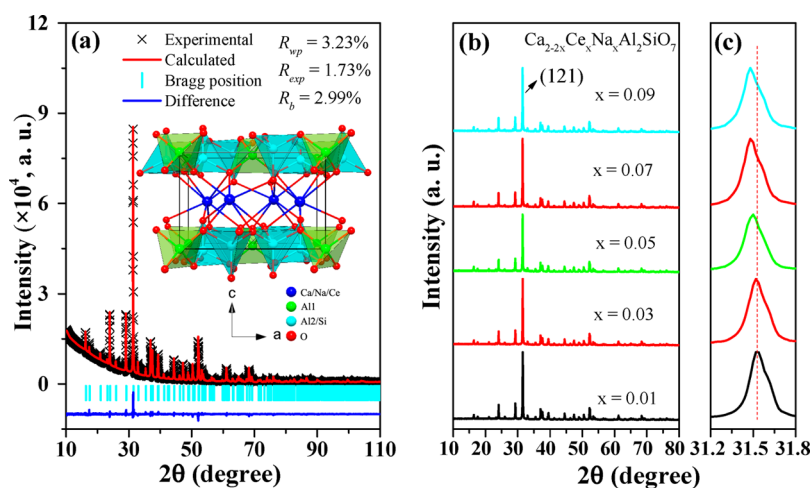


Figure 1. (a) Rietveld refinement for the powder XRD pattern of $\text{Ca}_{1.98}\text{Ce}_{0.01}\text{Na}_{0.01}\text{Al}_2\text{SiO}_7$ and a depiction of the unit cell structure in the inset; (b) XRD patterns and (c) diffraction peaks corresponding to (121) crystallographic plane of $\text{Ca}_{2-2x}\text{Ce}_x\text{Na}_x\text{Al}_2\text{SiO}_7$ ($x = 0.01, 0.03, 0.05, 0.07, 0.09$) samples at RT.

systematically. We focus on the composition-dependent $f-d$ transition energies and luminescence thermal stability of Ce^{3+} , showing that the lowest 5d levels of Ce^{3+} shift toward higher energies with increasing Sr^{2+} contents. In addition we found uplifts of the valence band maximum (VBM) and the CBM, leading to different thermal stability. These findings are interpreted and further understood by construction of vacuum referred binding energy (VRBE) schemes. The work provides an approach to understanding the composition-dependent thermal stability of luminescence and a clue for the future design of advanced phosphors.

2. EXPERIMENTAL SECTION

Powder samples of $\text{Ca}_{2-2x}\text{Ce}_x\text{Na}_x\text{Al}_2\text{SiO}_7$ ($x = 0.01, 0.03, 0.05, 0.07, 0.09$), $\text{Ca}_{1.98-y}\text{Sr}_y\text{Ce}_{0.01}\text{Na}_{0.01}\text{Al}_2\text{SiO}_7$, and $\text{Ca}_{1.98-y}\text{Sr}_y\text{Eu}_{0.01}\text{Na}_{0.01}\text{Al}_2\text{SiO}_7$ ($y = 0, 0.50, 1.00, 1.50, 1.98$) were synthesized by a high temperature solid-state reaction technique. Due to the mismatch of electrical charge between trivalent Ce^{3+} and divalent $\text{Ca}^{2+}/\text{Sr}^{2+}$, the monovalent Na^+ ions from Na_2CO_3 are introduced as electrical compensators. The details of preparation and characterization are described in the Supporting Information.

2.1. Phase Identification and Structure Analysis. Figure 1a shows the Rietveld refinement of the representative $\text{Ca}_{1.98}\text{Ce}_{0.01}\text{Na}_{0.01}\text{Al}_2\text{SiO}_7$ sample implemented with tetragonal $\text{Ca}_2\text{Al}_2\text{SiO}_7$ (ICSD 66740) as the initial model.¹⁸ The obtained fitting parameters are $R_{\text{wp}} = 3.23\%$, $R_{\text{exp}} = 1.73\%$, and $R_b = 2.99\%$, indicating that the refined results are reliable. Our sample forms a single phase with the $P4_2/m$ (113) space group, whose lattice parameters are $a = b = 7.6710(1)$ Å, $c = 5.0605(1)$ Å, $\alpha = \beta = \gamma = 90^\circ$, $V = 297.78(1)$ Å³, and $Z = 2$. Table S1 shows the final refined structural parameters. There are two kinds of Al^{3+} at different Wyckoff positions, i.e., AlI at 2a and AlII at 4e. The AlII shares one half of its crystallographic sites with Si. All AlI, AlII, and Si ions coordinate respectively with four oxygen ions to form AlO_4 and $(\text{Al,Si})\text{O}_4$ tetrahedrons that further connect with each other to construct the rigid layers of anionic groups via corner sharing approximately along the ab -plane. In addition, the layer of Ca^{2+} ions inserts between the layers of anionic groups to produce a sandwich-structural unit cell as shown in the inset of Figure 1a. Then along the c -axis the structure of the compound is softer than that along the ab -plane, because of the lack of protection of the rigid layers of anionic groups. Besides, there is only one type of Ca^{2+} site surrounded by eight neighboring O^{2-} ions to form a CaO_8 dodecahedron with C_2 symmetry, which can be approximately regarded as a distorted Thompson cube. The average $\text{Ca}/\text{Ce}-\text{O}$ bond distance is ~ 2.562 Å (256.2 pm), and the distance of the two

nearest adjacent $\text{Ca}-\text{Ca}$ is ~ 3.499 Å (349.9 pm). Considering the similar ionic radii at 8-fold coordination, Ce^{3+} (1.14 Å) and Na^+ (1.18 Å) ions are expected to occupy Ca^{2+} (1.12 Å) sites.²⁰ Figure 1b shows the $\text{Ce}^{3+}/\text{Na}^+$ concentration-dependent XRD patterns of $\text{Ca}_{2-2x}\text{Ce}_x\text{Na}_x\text{Al}_2\text{SiO}_7$ ($x = 0.01, 0.03, 0.05, 0.07, 0.09$) samples. All patterns are similar to each other and match well with the refinements. With a rise in doping concentration, the diffraction peaks of (121) crystallographic planes slightly shift toward the low-angle side as shown in Figure 1c. This phenomenon implies that slightly larger Ce^{3+} and Na^+ ions are effectively incorporated into the smaller Ca^{2+} sites, therefore resulting in the expansion of the unit cell with increasing $\text{Ce}^{3+}/\text{Na}^+$ concentration.

Figure 2a shows the XRD patterns of $\text{Ca}_{1.98-y}\text{Sr}_y\text{Ce}_{0.01}\text{Na}_{0.01}\text{Al}_2\text{SiO}_7$ ($y = 0, 0.50, 1.00, 1.50, 1.98$) samples. With increasing Sr^{2+} content, all

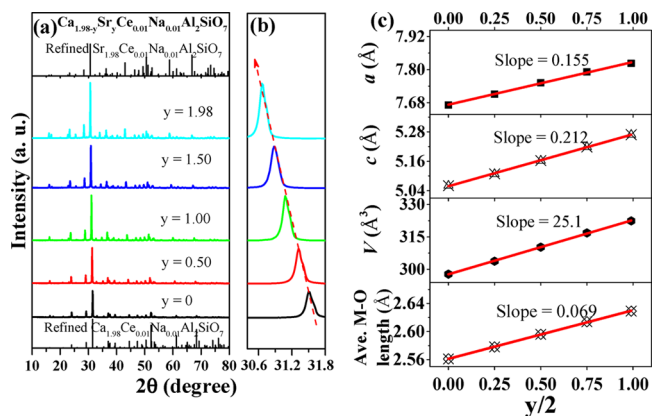


Figure 2. (a) XRD patterns and (b) diffraction peaks corresponding to (121) crystallographic planes of $\text{Ca}_{1.98-y}\text{Sr}_y\text{Ce}_{0.01}\text{Na}_{0.01}\text{Al}_2\text{SiO}_7$ ($y = 0, 0.50, 1.00, 1.50, 1.98$) at RT; (c) the linear fitting results of refined unit-cell parameters (a , b , and c), volumes (V), and average M–O ($M = \text{Ca}^{2+}, \text{Sr}^{2+}, \text{Ce}^{3+}, \text{Na}^+$) bond lengths with the mole ratio ($y/2$) of Sr^{2+} -doping concentration in $\text{Ca}_{1.98-y}\text{Sr}_y\text{Ce}_{0.01}\text{Na}_{0.01}\text{Al}_2\text{SiO}_7$.

diffraction peaks match well with the refined results, and no impurities have been detected. These phenomena indicate that the samples form continuous solid solutions. In addition, we notice that diffraction peaks of (121) crystallographic planes systematically shift toward the low-angle side with increasing Sr^{2+} concentration as shown in Figure 2b, because the incorporation of the larger radii Sr^{2+} (1.26 Å) results in an expansion of the dodecahedron and the unit cell.²⁰ This is confirmed by the monotonous increase of the refined unit-cell parameters,

volumes, and average M–O (M = Ca²⁺, Sr²⁺, Ce³⁺, Na⁺) bond lengths as observed in Figure 2c and Table S2. It should be noted that the Sr²⁺ content has linear contributions to the above parameters due to the isomorphic properties of Ca₂Al₂SiO₇ and Sr₂Al₂SiO₇, sticking to Vegard's law. Moreover, we find that the linearly fitted slope of the unit-cell parameter *c* (0.212) with the mole ratio (*y*/2) of Sr²⁺-doping concentration is larger than that of *a* and *b* (0.155), indicating that Sr²⁺ substituting for Ca²⁺ results in a more obvious expansion of the unit cell along the *c*-axis due to the softness between layers as discussed in Figure 1a. According to Table S3, we also know that the expansion of SrO₈ is not isotropic comparing with the initial CaO₈ polyhedron. These phenomena suggest that the doping of Sr²⁺ ions leads to a slight expansion and distortion of cation sites, which is expected to have influences on luminescence properties of Ce³⁺-doped (Ca, Sr)₂Al₂SiO₇.

2.2. VUV–UV–Vis Luminescence of Ca_{1.98}Ce_{0.01}Na_{0.01}Al₂SiO₇.

Figure 3 shows the synchrotron radiation (SR) VUV–UV (line a)

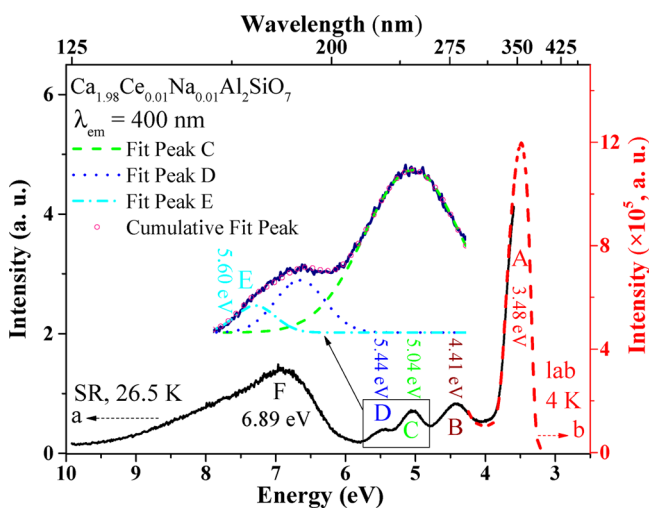


Figure 3. Synchrotron radiation VUV–UV (a, 26.5 K) and laboratory UV (b, 4 K) excitation spectra of Ca_{1.98}Ce_{0.01}Na_{0.01}Al₂SiO₇ of 400 nm emission. The inset shows the magnified spectrum in the region from 4.8 to 5.7 eV.

and laboratory UV (line b) excitation spectra of 400 nm emission at 26.5 and 4 K, correspondingly. Band F with a maximum at ~6.89 eV (180 nm) is attributed to the host absorption, corresponding to the excitation of an electron from the VBM to the host bound excitonic state. By adding the exciton binding energy (~8% of host absorption energy),²¹ the mobility band gap of Ca_{1.98}Ce_{0.01}Na_{0.01}Al₂SiO₇ is estimated to be ~7.44 eV, which is considered as the energy difference between the VBM and the CBM. This value falls between those of other silicates and aluminates, such as Lu₂SiO₅ (7.24 eV),²² LiY₉(SiO₄)₆O₂ (7.40 eV),⁵ Sr₃Al₂O₅Cl₂ (7.24 eV),²³ and Y₃Al₅O₁₂ (7.74 eV).²⁴

In addition, an intense excitation band A (at 3.48 eV, 356 nm) and three weaker ones (B, C, D) are observed in the lower energy region of spectra, and the peak maxima of these weaker bands are estimated to be 4.41 eV (B, 281 nm), 5.04 eV (C, 246 nm), and 5.44 eV (D, 228 nm), respectively. The peaks of the bands A, B, and C are close to the reported values (352, 279, and 248 nm),²⁵ while band D is undetected in the reference because of the too high temperature of measurement and too weak intensity of the xenon lamp below 250 nm. Above four excitation bands are attributed to the Ce³⁺ transitions from the 4f ground state to the different 5d_{*i*} states, respectively. In consideration of the low symmetry (*C_s*) of Ca²⁺ sites, it is expected that Ce³⁺ 5d states should be split into five 5d_{*i*} (*i* = 1–5) by the crystal field. The enlargement of the spectrum in the 4.8–5.7 eV region is exhibited in the figure inset. Another shoulder band E is observed at the high-energy side of band D with the energy maximum at ~5.60 eV (221

nm) based on three Gaussian functions (*R*² > 0.99), which is tentatively ascribed to the missed Ce³⁺ 5d₅ level.

The crystal-field splitting (CFS) energy of Ce³⁺ 5d states in Ca_{1.98}Ce_{0.01}Na_{0.01}Al₂SiO₇ is calculated to be 2.12 eV, which corresponds to the energy difference between Ce³⁺ 5d₅ and 5d₁ states. Generally, the CFS energy of Ce³⁺ in a specific site is directly associated with the average Ce–O bond length and the shape of coordination polyhedron, which can be scaled as

$$\epsilon_{\text{CFS}} = \beta \cdot R^{-2} \quad (1)$$

where ϵ_{CFS} is the CFS energy, β is dependent on the polyhedral shape, and *R* is the average Ce–O bond length.⁴ In the current case, taking $\beta = 1.07 \times 10^9 \text{ pm}^2 \text{ cm}^{-1}$ (8-coordinated dodecahedron) and *R* = 256.2 pm (mentioned in section 2.1), we obtain the calculated CFS energy $1.63 \times 10^4 \text{ cm}^{-1}$ (2.02 eV), which is consistent with the experimental one (2.12 eV). In addition, this experimental CFS energy is also close to the value of Ce³⁺ in CaSO₄ (2.24 eV),²⁶ Li₂CaSiO₄ (2.42 eV),²⁷ and LiCaPO₄ (1.98 eV)²⁷ where Ce³⁺ substitute Ca²⁺ ions in 8-coordinated dodecahedra. Therefore, the above discussions support our attribution of band E to be the Ce³⁺ 5d₅ level, and the CFS energy of Ce³⁺ 5d states is 2.12 eV.

The centroid of five Ce³⁺ 5d states, i.e., the average energy, is calculated to be 4.79 eV, which shifts down 1.56 eV with respect to ~6.35 eV in the gaseous state.³ This down-shift value is comparable to that in LiYSiO₄ (1.49 eV),²⁸ Lu₂Si₂O₇ (1.54 eV),⁴ YAlO₃ (1.57 eV),²⁹ and Y₃Al₅O₁₂ (1.63 eV),²⁴ showing that these silicates and aluminates have similar Ce³⁺–O²⁻ bond covalency, spectroscopic polarizability of anion, or nephelauxetic effect. Based on the discussed 8-coordinated dodecahedral shape and point symmetry (*C_s*) of sites, bands A and B can be further ascribed to the doublet nondegenerate E_g levels of the 5d orbit and bands C, D, and E to the 3-fold nondegenerate T_{2g} levels.^{7,30} In addition, the barycenter energies of E_g and T_{2g} levels are calculated to be 3.94 and 5.36 eV, respectively. The energy difference (0.85 eV) between the E_g barycenter and the 5d centroid is 1.49 eV times larger than that (0.57 eV) between the T_{2g} barycenter and the 5d centroid, which coincides with 1.5 times in distorted cubic coordination, since the CaO₈ dodecahedron can be approximately regarded as distorted Thompson cube as mentioned in section 2.1.⁷

Lastly, under excitation in the host absorption (180 nm) or in either of the five Ce³⁺ 5d states (220, 227, 245, 280, and 350 nm), all height-normalized emission spectra (26.5 K) overlap as shown in Figure S1, indicating that those bands originate from the same Ce³⁺ center and supporting the above band assignments.

Figure 4a shows the emission spectrum of Ca_{1.98}Ce_{0.01}Na_{0.01}Al₂SiO₇ under 356 nm excitation at 4 K in our lab, which appears slightly different from those measured in the SR VUV station at 26.5 K (Figure S1) due to the use of different setups of spectrometers as well as

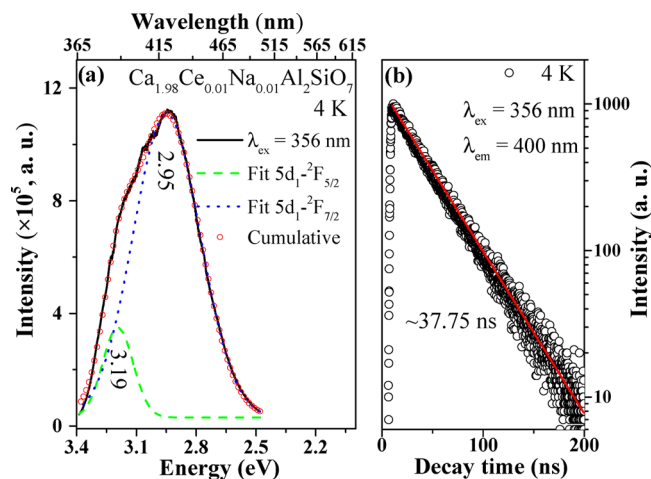


Figure 4. (a) Emission spectrum ($\lambda_{\text{ex}} = 356 \text{ nm}$) and (b) decay curve ($\lambda_{\text{ex}} = 356 \text{ nm}$, $\lambda_{\text{em}} = 400 \text{ nm}$) of Ca_{1.98}Ce_{0.01}Na_{0.01}Al₂SiO₇ at 4 K.

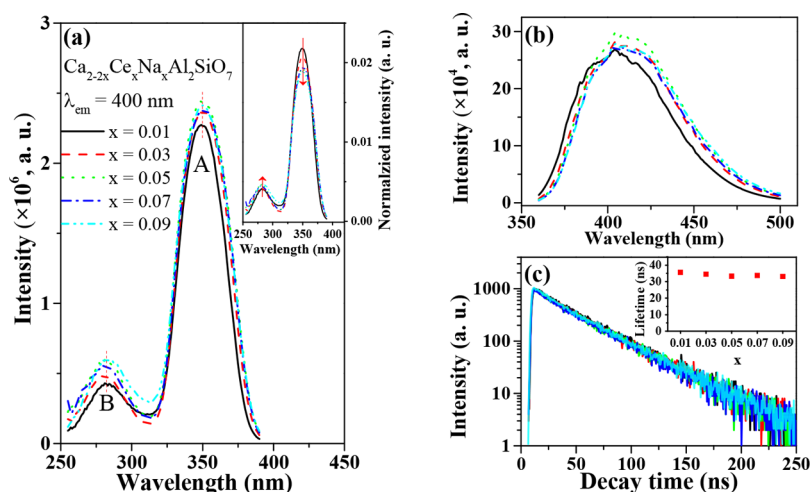


Figure 5. Ce^{3+} concentration-dependent (a) excitation ($\lambda_{\text{em}} = 400$ nm) and (b) emission ($\lambda_{\text{ex}} = 350$ nm) spectra, and (c) decay curve ($\lambda_{\text{ex}} = 350$ nm, $\lambda_{\text{em}} = 400$ nm) of $\text{Ca}_{2-2x}\text{Ce}_x\text{Na}_x\text{Al}_2\text{SiO}_7$ ($x = 0.01, 0.03, 0.05, 0.07, 0.09$) at RT. The inset in panel a corresponds to the intensity-normalized excitation spectra, while that in panel c corresponds to the Ce^{3+} -concentration dependent lifetime.

different measurement temperatures. A broad and asymmetric emission band with the maximum at 2.95 eV is observed and well-fitted with a sum of two Gaussian functions ($R^2 > 0.99$). Two Gaussian bands have maxima at about 3.19 and 2.95 eV, respectively, which are attributed to the transitions from the $\text{Ce}^{3+} 5d_1$ state to ${}^2F_{5/2}$ and ${}^2F_{7/2}$ spin-orbit multiplets. Then deriving from the energy difference between the band maxima of $4f-5d_1$ excitation and $5d_1-{}^2F_{5/2}$ emission, the Stokes shift of Ce^{3+} in our case is evaluated to be 0.29 eV ($2.34 \times 10^3 \text{ cm}^{-1}$), close to the most frequent cases ($2.20 \times 10^3 \text{ cm}^{-1}$).³¹ This result indicates that $\text{Ce}^{3+} 5d$ electrons in $\text{Ca}_2\text{Al}_2\text{SiO}_7$ experience a moderate effect of electron-phonon interaction with coordination environment. In addition, the luminescence decay curve of Ce^{3+} ($\lambda_{\text{ex}} = 356$ nm, $\lambda_{\text{em}} = 400$ nm) at 4 K strictly obeys the exponential characteristic with lifetime ~ 37.8 ns as shown in Figure 4b.

Figure 5a shows the Ce^{3+} concentration-dependent excitation spectra ($\lambda_{\text{em}} = 400$ nm) of $\text{Ca}_{2-2x}\text{Ce}_x\text{Na}_x\text{Al}_2\text{SiO}_7$ at RT. With the increase of doping content, the profile and peak remain almost unchanged because of the close radii between $\text{Ce}^{3+}/\text{Na}^+$ and Ca^{2+} ions. The intensity of band A seems to stabilize after $x = 0.03$, while that of band B keeps increasing with increasing Ce^{3+} content. After being normalized to the integrated intensity as shown in the inset, the relative intensity of band B to A increases with increasing doping concentration, which can be traced to the saturation effect of absorption. That is to say, the stronger absorption band A starts saturation at lower concentrations, which results in the relative intensity of the weaker absorption band B appearing to increase in the normalized spectra.⁸ In addition, band A gets slightly broadened at the long-wavelength side. This broadening increases the overlap between band A and the emission band, and therefore enlarges the strength of reabsorption and subsequently slightly shifts the emission band toward longer wavelengths as shown in Figure 5b. Figure 5c depicts the decay curves that all overlap to each other. The corresponding lifetimes are all about ~ 37.8 ns (the figure inset), indicating that there occurs no concentration quenching below $x = 0.09$.

2.3. VUV-UV-Vis Luminescence of $\text{Ca}_{1.98-y}\text{Sr}_y\text{Ce}_{0.01}\text{Na}_{0.01}\text{Al}_2\text{SiO}_7$. Figure 6a shows the Sr^{2+} -concentration dependent SR VUV-UV (solid) and lab UV (dash) excitation spectra of $\text{Ca}_{1.98-y}\text{Sr}_y\text{Ce}_{0.01}\text{Na}_{0.01}\text{Al}_2\text{SiO}_7$ ($y = 0, 0.50, 1.00, 1.50, 1.98$) of emission maxima at 26.5 and 4 K, respectively. The energies of $\text{Ce}^{3+} 5d_{1-5}$ states are summarized in rows 2–6 of Table 1. To estimate the energy of up-lying $\text{Ce}^{3+} 5d$ states as in the case of $\text{Ca}_{1.98}\text{Ce}_{0.01}\text{Na}_{0.01}\text{Al}_2\text{SiO}_7$, other four SR VUV-UV spectra ($y = 0.50-1.98$) were fitted according to three Gaussian functions ($R^2 > 0.99$) in the 4.8–5.7 eV region as shown in Figures S2–S5. Apparently the content of Sr^{2+} has a systematic influence on the positions of the $\text{Ce}^{3+} 4f-5d$ excitation bands in $\text{Ca}_{1.98-y}\text{Sr}_y\text{Ce}_{0.01}\text{Na}_{0.01}\text{Al}_2\text{SiO}_7$. With

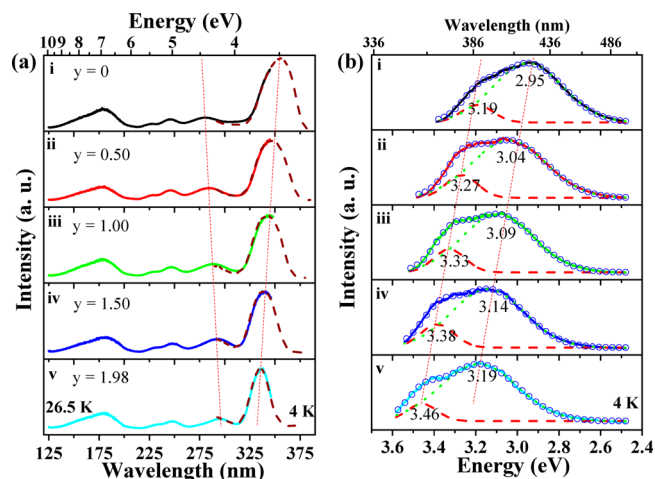


Figure 6. Sr^{2+} -concentration dependent (a) synchrotron radiation VUV-UV (solid, 26.5 K), laboratory UV (dash, 4 K) excitation, and (b) UV-vis emission (4 K) spectra of $\text{Ca}_{1.98-y}\text{Sr}_y\text{Ce}_{0.01}\text{Na}_{0.01}\text{Al}_2\text{SiO}_7$ ($y = 0, 0.50, 1.00, 1.50, 1.98$) of emission and excitation maxima, respectively.

the gradual replacement of Ca^{2+} by Sr^{2+} , the $4f-5d_1$ band shifts toward high energies by 0.21 eV accompanied by the shift of the $4f-5d_5$ by 0.04 eV and the $4f-5d_2$ by 0.18 eV toward low energies. The opposite shift of the $4f-5d_1$ and $4f-5d_5$ bands is because the increased Sr^{2+} enlarges the Ce-O coordination polyhedron and then reduces the CFS by 0.25 eV as shown in row 7 of Table 1. In addition, the various shifts of $5d_{2,3,4}$ may relate to the slight distortion of sites as mentioned in section 2.1. The substitution of Sr^{2+} for Ca^{2+} ions slightly and systematically shifts the host absorption toward lower energy (from 6.89 to 6.85, 6.84, 6.82, and 6.81 eV) as shown in row 9 of Table 1 or, in other words, slightly and continuously reduces the band gap energy (from 7.44 to 7.40, 7.39, 7.37, and 7.35 eV), while it exerts a limited influence on the $\text{Ce}^{3+} 5d$ centroid shift (from 1.56 to 1.58 eV, in row 8).

Figure 6b depicts the UV-vis emission spectra of $\text{Ca}_{1.98-y}\text{Sr}_y\text{Ce}_{0.01}\text{Na}_{0.01}\text{Al}_2\text{SiO}_7$ of excitation maxima at 4 K. Based on two Gaussian functions ($R^2 > 0.99$), all of the emission spectra were fitted and plotted in the figure, and the energies of $\text{Ce}^{3+} 5d_1-{}^2F_{5/2}$ emissions are summarized in row 10 of Table 1. We notice that the emission bands systematically shift toward the high-energy side with increasing Sr^{2+} concentration, like the behavior of $\text{Ce}^{3+} 5d_1$ states. The energy of zero phonon line (ZPL) is an important parameter to

Table 1. Energies of Ce³⁺ 4f–5d_{1–5} Excitation Bands, CFS, Centroid Shift $\epsilon_c(A)$, 5d_{1–2}F_{5/2} Emission Band, ZPL, Stokes Shift, and Host Absorption as Well as the Coulomb Repulsion Energy $U(6,A)$ in Ca_{1.98–y}Sr_yCe_{0.01}Na_{0.01}Al₂SiO₇ ($y = 0, 0.50, 1.00, 1.50, 1.98$)^a

property	$y = 0$	$y = 0.50$	$y = 1.00$	$y = 1.50$	$y = 1.98$
4f–5d ₁ excitation band	3.48	3.57	3.61	3.65	3.69
4f–5d ₂ excitation band	4.41	4.37	4.31	4.28	4.23
4f–5d ₃ excitation band	5.04	5.04	5.02	4.99	5.00
4f–5d ₄ excitation band	5.44	5.44	5.42	5.38	5.35
4f–5d ₅ excitation band	5.60	5.60	5.58	5.57	5.56
Ce ³⁺ 5d CFS	2.12	2.03	1.97	1.92	1.87
Ce ³⁺ 5d centroid shift	1.56	1.55	1.56	1.58	1.58
host absorption	6.89	6.85	6.84	6.82	6.81
5d _{1–2} F _{5/2} emission band	3.19	3.27	3.33	3.38	3.46
ZPL	3.31	3.38	3.43	3.49	3.55
Stokes shift	0.29	0.30	0.28	0.27	0.23
$U(6,A)$ ^b	6.84	6.84	6.83	6.82	6.82

^aAll energies are scaled as electronvolts (eV). ^bDerived from Ce³⁺ 5d centroid shift $\epsilon_c(A)$ via $U(6,A) = 5.44 + 2.834e^{-\epsilon_c(A)/2.2}$.^{21,32–34}

understand luminescence properties.^{8,35–37} According to the intersection point of the excitation and emission spectra as shown in Figure S6 and row 11 of Table 1,³⁷ the evaluated energy of the ZPL gradually increases by 0.24 eV, which is correlated to the increasing average Ce³⁺–O^{2–} bond length and is indeed comparable with the decreasing CFS (0.25 eV) with increasing Sr²⁺ content.

In addition, the derived Stokes shift is about 0.27 ± 0.04 eV as summarized in row 12 of Table 1. With increasing Sr²⁺ content, the Stokes shift almost keeps invariable and only roughly decreases about 0.06 eV. The observation seems to imply that the effect of electron–vibration interaction (EVI) is nearly unchanged at different Sr²⁺ contents. The 5d centroid shift, CFS, and EVI together decide the position of Ce³⁺ emission.³⁷ Therefore, the shift of emission toward shorter wavelengths in the current case mainly results from the contribution of a reduced CFS of Ce³⁺ 5d states, while the EVI effect only imposes a limited contribution.

Figure 7 exhibits decay curves of Ca_{1.98–y}Sr_yCe_{0.01}Na_{0.01}Al₂SiO₇ of excitation and emission maxima at 4 K. All decay curves obey the

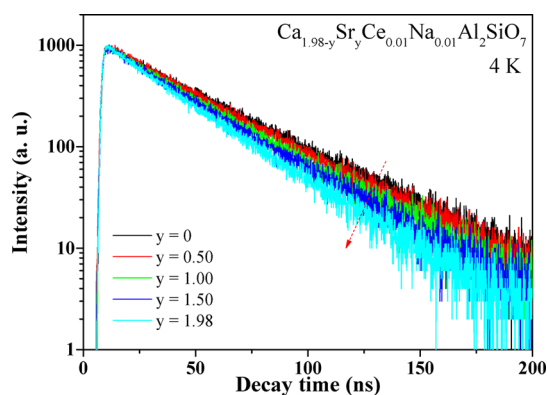


Figure 7. Sr²⁺-concentration dependent decay curves (4 K) of Ca_{1.98–y}Sr_yCe_{0.01}Na_{0.01}Al₂SiO₇ ($y = 0, 0.50, 1.00, 1.50, 1.98$) of excitation and emission maxima.

exponential characteristic and show a faster decay rate with increasing Sr²⁺ content. The corresponding radiative lifetime has a sequential decrease ($\sim 25\%$) from ~ 37.8 to 35.1, 33.0, 31.1, and 28.3 ns. This reduction of lifetime can be qualitatively understood via the polarization effect or usually termed as a local-field effect that has been used to interpret the various lifetimes of the Ce³⁺³⁸ and Pr³⁺³⁹ f–d emissions in different media with the following formulas:

$$\frac{1}{\tau_r} = \frac{4.34 \times 10^{17} |\langle 5d|r|4f \rangle_{\text{eff}}|^2 \chi}{\lambda^3} \quad (2)$$

$$\chi = n[(n^2 + 2)/3]^2 \quad (3)$$

where τ_r is the radiative lifetime (in seconds), λ is the average emission wavelength (in nanometers) in a given host, $\langle 5d|r|4f \rangle_{\text{eff}}$ represents the effective radial integral with best-fit value 0.0281 nm for Ce³⁺, and χ is the refractive index (n) dependent factor related to the virtual-cavity model. Based on the above equations, the radiative lifetime positively correlates to the cube of the emission wavelength. The shorter the Ce³⁺ emission wavelength, the shorter the lifetime of 5d electrons. It is indeed the fact when increasing Sr²⁺ content as shown in Figures 6b and 7. In addition, the radiative lifetime is anticorrelated to the refractive index of the samples. According to the additive scheme,⁴⁰ the mean refractive index of the majority of complex oxides can be estimated within 5% error. In the current case the estimated refractive index has a limited increase $\sim 0.86\%$ corresponding to $\sim 0.60\%$ decrease of $1/\chi$, therefore confirming that the influence of refractive index on the decrease of lifetime is insignificant, instead, it is the shift of emissions toward the short-wavelength side that takes the dominant responsibility.

At RT we also measured Sr²⁺-concentration dependent UV–vis emission spectra of Ca_{1.98–y}Sr_yCe_{0.01}Na_{0.01}Al₂SiO₇ of excitation maxima in order to compare their intensities under the same conditions as shown in Figure S7a. Except for the experimental point $y = 1.00$, whose intensity is unexpectedly stronger than that of $y = 0.50$ because of possible error of experiment, the integrated intensity has a significant decrease beyond $y = 0.50$, which keeps in line with the result of the measured internal quantum efficiency decreasing from 78.7% to 77.0%, 61.6%, 47.2%, and 29.7%. More importantly, after $y = 0.50$ the corresponding decay curves also gradually deviate from the single-exponential characteristic as shown in Figure S7b. The above phenomena point out a fact that highly doping Sr²⁺ ($y > 0.50$) into Ca₂Al₂SiO₇ can open a thermal-quenching channel at RT for Ce³⁺ 5d electrons, which may influence their thermal stability.

2.4. Temperature-Dependent Luminescence of M_{1.98}Ce_{0.01}Na_{0.01}Al₂SiO₇ (M = Ca, Sr). Figure S8 shows the temperature-dependent (77–500 K) integrated emission intensities of M_{1.98}Ce_{0.01}Na_{0.01}Al₂SiO₇ (M = Ca, Sr). They suffer from significant decreases with increasing temperature, and 50% of them are left at ~ 470 K (i.e., thermal-quenching temperature, $T_{50\%}$) for Ca_{1.98}Ce_{0.01}Na_{0.01}Al₂SiO₇ and at ~ 340 K for Sr_{1.98}Ce_{0.01}Na_{0.01}Al₂SiO₇. Figure S9 shows their temperature-dependent decay curves. Below specific temperatures (320 vs 250 K), they all obey the single-exponential characteristic and subsequently deviate because of thermal quenching. The corresponding average fluorescence lifetimes of Ce³⁺ at different temperatures are exhibited in Figure 8, in which the average lifetime (τ) is estimated by adopting the following formula:

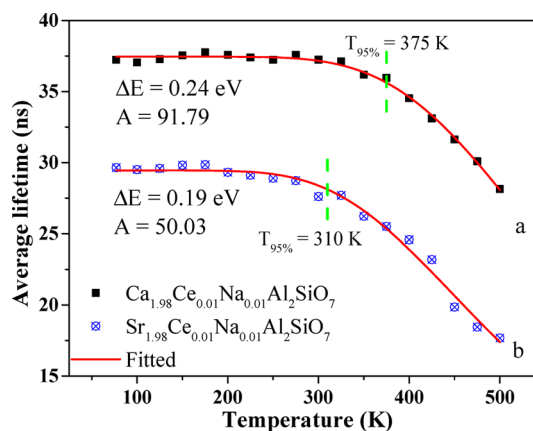


Figure 8. Temperature-dependent average lifetime of Ca_{1.98}Ce_{0.01}Na_{0.01}Al₂SiO₇ (a) and Sr_{1.98}Ce_{0.01}Na_{0.01}Al₂SiO₇ (b).

$$\tau = \frac{\int_0^{\infty} tI(t) dt}{\int_0^{\infty} I(t) dt} \quad (4)$$

where $I(t)$ is the emission intensity after pulsed excitation and $I(0)$ is the emission intensity at $t = 0$. It can be seen that the lifetime of Ce^{3+} emission in $\text{Ca}_2\text{Al}_2\text{SiO}_7$ is longer than that in $\text{Sr}_2\text{Al}_2\text{SiO}_7$ at overall specific temperatures because of the longer emission wavelength as mentioned in section 2.3. Besides, the onset temperature of thermal quenching ($T_{95\%}$) is estimated at 375 K for $\text{Ca}_{1.98}\text{Ce}_{0.01}\text{Na}_{0.01}\text{Al}_2\text{SiO}_7$, and that at 310 K for $\text{Sr}_{1.98}\text{Ce}_{0.01}\text{Na}_{0.01}\text{Al}_2\text{SiO}_7$. When we consider that quenching is mainly caused by thermal ionization of Ce^{3+} 5d electrons to the conduction band (CB) as proposed in Ce^{3+} -doped garnets,^{41–43} Ln_2O_3 ($\text{Ln} = \text{Y}, \text{Lu}, \text{La}$),⁴⁴ Lu_2SiO_5 ,⁴⁴ and GdAlO_3 ,⁴⁵ the activation energy ΔE of thermal quenching can be derived from the single-barrier quenching model, eq 5,

$$\Gamma(T) = \Gamma(0) \left[1 + A \exp\left(-\frac{\Delta E}{kT}\right) \right]^{-1} \quad (5)$$

where $\Gamma(T)$ and $\Gamma(0)$ denote the decay time at temperature T and 0 K, correspondingly, A is a pre-exponential factor indicating the rate constant for the thermally activated escape, and k is the Boltzmann constant [$8.6173324(78) \times 10^{-5}$ eV/K]. The fitting curves are plotted as red lines in Figure 8. We obtain ΔE 0.24 eV (A 91.79) for $\text{Ca}_{1.98}\text{Ce}_{0.01}\text{Na}_{0.01}\text{Al}_2\text{SiO}_7$ and 0.19 eV (A 50.03) for $\text{Sr}_{1.98}\text{Ce}_{0.01}\text{Na}_{0.01}\text{Al}_2\text{SiO}_7$, in which the larger value of the former is consistent with its much higher $T_{50\%}$ and $T_{95\%}$ compared with those of the latter as displayed in Figures S8 and 8.

In addition, the difference in ΔE and $T_{50\%}$ can be understood through the electronic structure from the VRBE scheme for Ln^{3+} 4f and 4f^{*n*-1}5d states and Ln^{2+} 4f states in hosts. In the next section, we will discuss the $\text{Eu}^{3+}-\text{O}^{2-}$ charge-transfer states (CTS) of $\text{Ca}_{1.98-y}\text{Sr}_y\text{Eu}_{0.01}\text{Na}_{0.01}\text{Al}_2\text{SiO}_7$ and construct the VRBE schemes for these compounds.

2.5. The Energy of the $\text{Eu}^{3+}-\text{O}^{2-}$ Charge-Transfer State of $\text{Ca}_{1.98-y}\text{Sr}_y\text{Eu}_{0.01}\text{Na}_{0.01}\text{Al}_2\text{SiO}_7$ and the Construction of VRBE Schemes. Figure S10 exhibits the Sr^{2+} concentration-dependent XRD patterns of $\text{Ca}_{1.98-y}\text{Sr}_y\text{Eu}_{0.01}\text{Na}_{0.01}\text{Al}_2\text{SiO}_7$ ($y = 0, 0.50, 1.00, 1.50, 1.98$) samples with single-phase purities. The height-normalized emission spectra under excitation at 265 nm in Figure S11 presents the typical $^3\text{D}_0 \rightarrow ^7\text{F}_j$ ($J = 0-4$) transitions of Eu^{3+} ions. Figure 9 shows their height-normalized VUV–UV excitation spectra by monitoring 616 nm emission of Eu^{3+} $^5\text{D}_0 \rightarrow ^7\text{F}_2$ transition at 26.5 K. In the 4.0–6.5 eV energy range, the intense and broad excitation bands are ascribed to transitions of $\text{Eu}^{3+}-\text{O}^{2-}$ CTS with peak energies from 4.97 to 4.94, 4.92, 4.88, and 4.79 eV in the order of increasing Sr^{2+} content, in which the first and last values are slightly larger than those of the

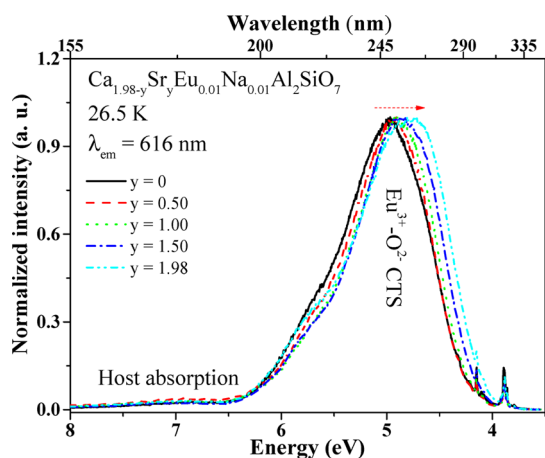


Figure 9. Sr^{2+} concentration-dependent VUV–UV excitation spectra of $\text{Ca}_{1.98-y}\text{Sr}_y\text{Eu}_{0.01}\text{Na}_{0.01}\text{Al}_2\text{SiO}_7$ ($y = 0, 0.50, 1.00, 1.50, 1.98$) of 616 nm emission at 26.5 K.

reported ones (4.88 eV in $\text{Ca}_{1.86}\text{Al}_2\text{SiO}_7:0.14\text{Eu}^{3+}$ and 4.73 eV in $\text{Sr}_{1.86}\text{Al}_2\text{SiO}_7:0.14\text{Eu}^{3+}$) measured at RT and higher doping concentration.⁴⁶ On the other hand, the narrow lines on the lower energies and very weak broad bands on another side are attributed to f–f transitions of Eu^{3+} ions and host absorptions, respectively. With increasing Sr^{2+} content, the energy of $\text{Eu}^{3+}-\text{O}^{2-}$ CTS systematically reduces by 0.18 eV. This decreasing energy is dominantly arising from the increased average bond length between center and ligand ions in host when increasing Sr^{2+} concentration. Similar phenomena have been noticed in previous reports,^{47,48} and attributed to a smaller Madelung potential. That is to say, an increase in distance between center ions and nearby ligands decreases their mutual repulsion of electrons, and then reduces the energy difference between the VBM and the ground state of Eu^{2+} . Therefore, it can be expected that the VBM would move upward when increasing Sr^{2+} content because the vacuum referred electron binding energy of the Eu^{2+} ground state is always found to be located at around -4 eV in the chemical shift model of oxides.^{21,32–34,49}

Based on the energies of (i) the Ce^{3+} 4f–5d₁ transition (row 2 of Table 1), (ii) the Ce^{3+} 5d centroid shift (row 8 of Table 1) and the derived Coulomb repulsion energy $U(6A)$ (row 13 of Table 1), (iii) the host absorption (row 9 of Table 1), and (iv) the $\text{Eu}^{3+}-\text{O}^{2-}$ CTS, we construct the stacked VRBE schemes of $\text{Ca}_{2-y}\text{Sr}_y\text{Al}_2\text{SiO}_7$ ($y = 0, 0.5, 1.0, 1.5, 2.0$) as shown in Figure 10.^{21,32–34,50} According to these

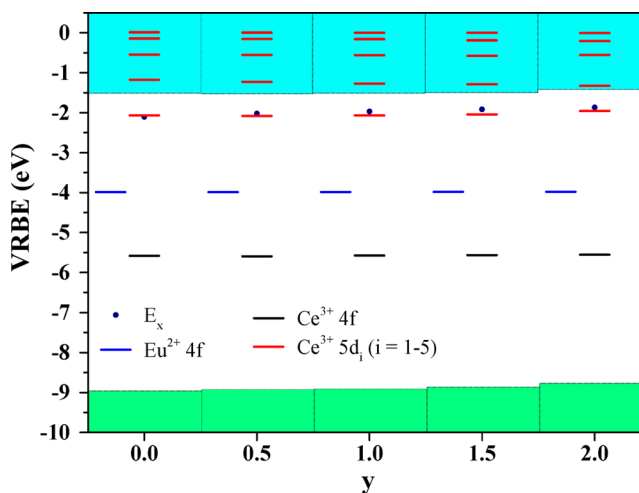


Figure 10. VRBE schemes of $\text{Ca}_{2-y}\text{Sr}_y\text{Al}_2\text{SiO}_7$ ($y = 0, 0.5, 1.0, 1.5, 2.0$) with location of $\text{Ce}^{3+}/\text{Eu}^{2+}$ 4f and Ce^{3+} 5d₁ states. E_x represents the binding energy at the host exciton creation, while the cyan (top) and green (bottom) rectangles represent the conduction band and the valence band, respectively.

VRBE schemes, the energies of Ce^{3+} and Eu^{2+} 4f ground states keep almost invariable due to the shielding effect of the outer filled 5s² and 5p⁶ orbitals, but the VBM and the CBM as well as the Ce^{3+} 5d₁ state move upward with increasing Sr^{2+} content. The uplift of the VBM and CBM is mainly arising from a smaller Madelung potential as mentioned above, while that of the Ce^{3+} 5d₁ state is dominantly ascribed to a decreased CFS induced by increased Sr^{2+} content.

The discussed luminescence of Ce^{3+} -doped $(\text{Ca},\text{Sr})_2\text{Al}_2\text{SiO}_7$ in the above sections can be further understood by these VRBE schemes. First, except for Ce^{3+} 5d₁ level locating within the band gap, 5d_{2–5} states in $(\text{Ca},\text{Sr})_2\text{Al}_2\text{SiO}_7:\text{Ce}^{3+}$ have immersed into the CB according to VRBE schemes, resulting in easy thermal ionization of 5d electrons and the much weaker intensities of 4f–5d_{2–5} transitions than that of 4f–5d₁ as shown in the VUV–UV excitation spectra even at low temperature (see Figures 3 and 6a). Second, the experimental ΔE and $T_{50\%}$ of $\text{Ca}_{1.98}\text{Ce}_{0.01}\text{Na}_{0.01}\text{Al}_2\text{SiO}_7$ are much larger than those of $\text{Sr}_{1.98}\text{Ce}_{0.01}\text{Na}_{0.01}\text{Al}_2\text{SiO}_7$ as shown in Figures 8 and S8, which also can be understood via Figure 10. The competitive uplifts of Ce^{3+} 5d₁ level and the CBM result in an overall decrease of their energy difference

(0.59 eV for $\text{Ca}_{1.98}\text{Ce}_{0.01}\text{Na}_{0.01}\text{Al}_2\text{SiO}_7$ first and 0.45 eV for $\text{Sr}_{1.98}\text{Ce}_{0.01}\text{Na}_{0.01}\text{Al}_2\text{SiO}_7$ at last) with increasing Sr^{2+} concentration, indicating that $\text{Ca}_{1.98}\text{Ce}_{0.01}\text{Na}_{0.01}\text{Al}_2\text{SiO}_7$ has a larger barrier of thermal quenching through thermal ionization of 5d electrons to the CB so that it owns a better thermal stability. While Sr^{2+} can reduce this barrier, it therefore leads to a worse thermal stability of $\text{Sr}_{1.98}\text{Ce}_{0.01}\text{Na}_{0.01}\text{Al}_2\text{SiO}_7$.

2.6. X-ray Excited Luminescence. Lastly, to evaluate the possibility of $(\text{Ca,Sr})_2\text{Al}_2\text{SiO}_7:\text{Ce}^{3+}$ as a scintillation material, the X-ray excited luminescence spectra and scintillation light yield of $\text{Ca}_{1.98-y}\text{Sr}_y\text{Ce}_{0.01}\text{Na}_{0.01}\text{Al}_2\text{SiO}_7$ ($y = 0, 1.98$) were studied as shown in Figure 11. Under X-ray excitation the as-prepared samples give broad

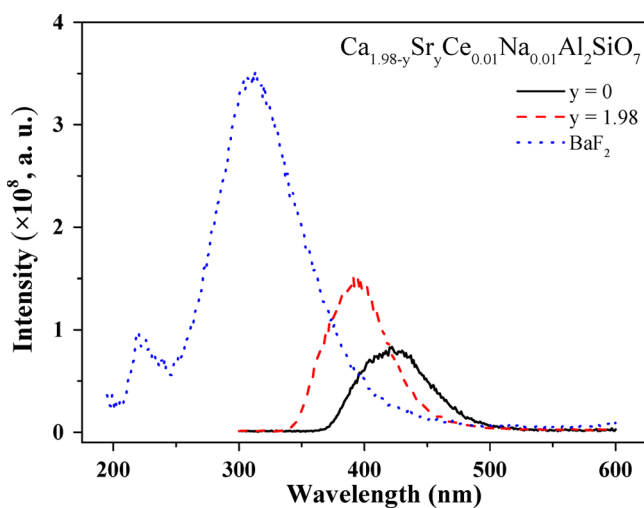


Figure 11. X-ray excited luminescence spectra of $\text{Ca}_{1.98-y}\text{Sr}_y\text{Ce}_{0.01}\text{Na}_{0.01}\text{Al}_2\text{SiO}_7$ ($y = 0, 1.98$) and a reference sample BaF_2 at RT.

and featureless emission bands at ~ 420 ($y = 0$) and 393 nm ($y = 1.98$) due to Ce^{3+} $5d_1-4f$ transitions. They keep in line with the RT emission spectra in Figure S7a, with slight differences in emission peaks as a result of different detector and instrument responses. Deriving from the integrated intensity, the light yields are estimated to be only ~ 1500 and 2500 photon/MeV for the $y = 0$ and 1.98 samples, correspondingly, in which BaF_2 (8800 photon/MeV) is used as the reference. Although the light yield has a significant increase ($\sim 67\%$) after doping Sr^{2+} because of the larger density (see row 6 of Table S2) facilitating the absorption of X-ray radiation, however, the low light yield of the studied samples implies that they are not suitable as scintillators.

3. CONCLUSION

In summary, we have systematically studied the effect of Ce^{3+} and $\text{Ca}^{2+}/\text{Sr}^{2+}$ on the crystal structure evolution and luminescence properties, including $4f-5d$ transition energies, radiative lifetime, emission intensity, quantum efficiency, and thermal stability, of Ce^{3+} -doped $(\text{Ca,Sr})_2\text{Al}_2\text{SiO}_7$ through Rietveld refinement and VUV-UV-vis spectra. In $\text{Ca}_2\text{Al}_2\text{SiO}_7:\text{Ce}^{3+}$, the host absorption (6.89 eV) and five Ce^{3+} 5d states are identified, and the band gap and Ce^{3+} 5d CFS and centroid shift are estimated to be 7.44, 2.12, and 1.56 eV, respectively. With the gradual substitution of Sr^{2+} for Ca^{2+} ions, the cation sites experience a slight expansion and distortion leading to a sequential decrease of Ce^{3+} 5d CFS (0.25 eV) and the systematical shift of the $4f-5d$ excitation and emission bands. Meanwhile, the lifetime of Ce^{3+} 5d electrons has a continuous decrease ($\sim 25\%$) because of the shift of emission. In comparison with the CFS, the change of cations and

structure slightly reduces the band gap only, while its influence on Ce^{3+} 5d centroid shift almost can be neglected.

Moreover, highly doping Sr^{2+} ($y > 0.50$) can open a thermal-quenching channel at RT for $\text{Ca}_{1.98-y}\text{Sr}_y\text{Ce}_{0.01}\text{Na}_{0.01}\text{Al}_2\text{SiO}_7$, mainly thermal ionizing of 5d electrons to CB, therefore resulting in the much lower emission intensity, quantum efficiency, activation energy, and thermal-quenching temperature of $\text{Sr}_{1.98}\text{Ce}_{0.01}\text{Na}_{0.01}\text{Al}_2\text{SiO}_7$ than those of $\text{Ca}_{1.98}\text{Ce}_{0.01}\text{Na}_{0.01}\text{Al}_2\text{SiO}_7$. Before constructing VRBE schemes, the energy of $\text{Eu}^{3+}-\text{O}^{2-}$ CTS in $(\text{Ca,Sr})_2\text{Al}_2\text{SiO}_7:\text{Eu}^{3+}$ has been discussed, and its shift toward the low-energy side is because of the effect of the increased Sr^{2+} on the decreased Madelung potential, which also results in the slight uplift for the VBM and the CBM. In combination with VUV-UV spectra and VRBE schemes, the effect of Sr^{2+} on the deteriorated thermal stability is understood and ascribed to the fact that it reduces Ce^{3+} 5d CFS and then the barrier of thermal quenching in $(\text{Ca,Sr})_2\text{Al}_2\text{SiO}_7$. In addition, except for the Ce^{3+} $5d_1$ state located within the band gap, $5d_{2-5}$ states in $(\text{Ca,Sr})_2\text{Al}_2\text{SiO}_7$ have immersed into the CB according to VRBE schemes, therefore leading to the much weaker intensities of Ce^{3+} $4f-5d_{2-5}$ transitions than that of $4f-5d_1$. Lastly, the light yield of as-prepared samples under X-ray radiation has a remarkable increase ($\sim 67\%$) after Sr^{2+} replacement, however, their overall low light yields imply that they are not suitable as scintillators.

■ ASSOCIATED CONTENT

Supporting Information

The Supporting Information is available free of charge on the ACS Publications website at DOI: 10.1021/acs.inorgchem.7b01939.

Details of sample preparation and characterization, final refined structural parameters, bond distances, emission, VUV-UV, and UV spectra, ZPL, and XRD patterns (PDF)

■ AUTHOR INFORMATION

Corresponding Author

*E-mail: cesbin@mail.sysu.edu.cn. Phone: +86-20-84113695. Fax: +86-20-84111038.

ORCID

Litian Lin: 0000-0003-3241-2651

Rui Shi: 0000-0002-3120-0596

Hongbin Liang: 0000-0002-3972-2049

Notes

The authors declare no competing financial interest.

■ ACKNOWLEDGMENTS

This work has been financially supported by the National Natural Science Foundation of China (U1432249, U1632101 and 21671201), and the Science and Technology Project of Guangdong Province (2017A010103034).

■ REFERENCES

- (1) Qin, X.; Liu, X.; Huang, W.; Bettinelli, M.; Liu, X. Lanthanide-activated phosphors based on $4f-5d$ optical transitions: Theoretical and experimental aspects. *Chem. Rev.* **2017**, *117*, 4488–4527.
- (2) Zhou, L.; Zhou, W.; Pan, F.; Shi, R.; Huang, L.; Liang, H.; Tanner, P. A.; Du, X.; Huang, Y.; Tao, Y.; Zheng, L. Spectral Properties and Energy Transfer of a Potential Solar Energy Converter. *Chem. Mater.* **2016**, *28*, 2834–2843.

- (3) Dorenbos, P. 5d-level energies of Ce³⁺ and the crystalline environment. I. Fluoride compounds. *Phys. Rev. B: Condens. Matter Mater. Phys.* **2000**, *62*, 15640.
- (4) Dorenbos, P. 5d-level energies of Ce³⁺ and the crystalline environment. III. Oxides containing ionic complexes. *Phys. Rev. B: Condens. Matter Mater. Phys.* **2001**, *64*, 125117.
- (5) Zhou, W.; Pan, F.; Zhou, L.; Hou, D.; Huang, Y.; Tao, Y.; Liang, H. Site Occupancies, Luminescence, and Thermometric Properties of LiY₉(SiO₄)₆O₂:Ce³⁺ Phosphors. *Inorg. Chem.* **2016**, *55*, 10415–10424.
- (6) Zhang, L.; Zhang, J.; Pan, G.-H.; Zhang, X.; Hao, Z.; Luo, Y.; Wu, H. Low-Concentration Eu²⁺-Doped SrAlSi₄N₇:Ce³⁺ Yellow Phosphor for wLEDs with Improved Color-Rendering Index. *Inorg. Chem.* **2016**, *55*, 9736–9741.
- (7) Setlur, A. A.; Heward, W. J.; Gao, Y.; Srivastava, A. M.; Chandran, R. G.; Shankar, M. V. Crystal chemistry and luminescence of Ce³⁺-doped Lu₂CaMg₂(Si,Ge)₃O₁₂ and its use in LED based lighting. *Chem. Mater.* **2006**, *18*, 3314–3322.
- (8) Bachmann, V.; Ronda, C.; Meijerink, A. Temperature quenching of yellow Ce³⁺ luminescence in YAG: Ce. *Chem. Mater.* **2009**, *21*, 2077–2084.
- (9) Holloway, W.; Kestigian, M. Optical properties of cerium-activated garnet crystals. *J. Opt. Soc. Am.* **1969**, *59*, 60–63.
- (10) Ueda, J.; Kuroishi, K.; Tanabe, S. Bright persistent ceramic phosphors of Ce³⁺-Cr³⁺-codoped garnet able to store by blue light. *Appl. Phys. Lett.* **2014**, *104*, 101904.
- (11) Xia, Z.; Meijerink, A. Ce³⁺-Doped garnet phosphors: composition modification, luminescence properties and applications. *Chem. Soc. Rev.* **2017**, *46*, 275–299.
- (12) Jary, V.; Nikl, M.; Kurosawa, S.; Shoji, Y.; Mihokova, E.; Beitlerova, A.; Pazzi, G. P.; Yoshikawa, A. Luminescence characteristics of the Ce³⁺-doped pyrosilicates: The case of La-admixed Gd₂Si₂O₇ single crystals. *J. Phys. Chem. C* **2014**, *118*, 26521–26529.
- (13) Kamada, K.; Endo, T.; Tsutumi, K.; Yanagida, T.; Fujimoto, Y.; Fukabori, A.; Yoshikawa, A.; Pejchal, J.; Nikl, M. Composition engineering in cerium-doped (Lu,Gd)₃(Ga,Al)₅O₁₂ single-crystal scintillators. *Cryst. Growth Des.* **2011**, *11*, 4484–4490.
- (14) Shang, M.; Fan, J.; Lian, H.; Zhang, Y.; Geng, D.; Lin, J. A double substitution of Mg²⁺-Si⁴⁺/Ge⁴⁺ for Al(1)₃₊-Al(2)₃₊ in Ce³⁺-doped garnet phosphor for white LEDs. *Inorg. Chem.* **2014**, *53*, 7748–7755.
- (15) Lin, H.; Xu, J.; Huang, Q.; Wang, B.; Chen, H.; Lin, Z.; Wang, Y. Bandgap tailoring via Si doping in inverse-garnet Mg₃Y₂-Ge₃O₁₂:Ce³⁺ persistent phosphor potentially applicable in AC-LED. *ACS Appl. Mater. Interfaces* **2015**, *7*, 21835–21843.
- (16) Ogieglo, J. M.; Katelnikovas, A.; Zych, A.; Jüstel, T.; Meijerink, A.; Ronda, C. R. Luminescence and luminescence quenching in Gd₃(Ga,Al)₅O₁₂ scintillators doped with Ce³⁺. *J. Phys. Chem. A* **2013**, *117*, 2479–2484.
- (17) Liu, B.; Shi, C.; Yin, M.; Fu, Y.; Zhang, G.; Ren, G. Luminescence and energy transfer processes in Lu₂SiO₅:Ce³⁺ scintillator. *J. Lumin.* **2006**, *117*, 129–134.
- (18) Kimata, M.; Shimizu, M.; Saito, S. Refinement of the high-temperature crystal structure of gehlenite using a new radiative air-cooled heater. *Trans. Am. Crystallogr. Assoc.* **1991**, *27*, 301–308.
- (19) Zhang, Q.; Wang, J.; Zhang, M.; Su, Q. Tunable bluish green to yellowish green Ca₂(1-x)Sr_{2x}Al₂SiO₇:Eu²⁺ phosphors for potential LED application. *Appl. Phys. B: Lasers Opt.* **2008**, *92*, 195–198.
- (20) Shannon, R. D. Revised effective ionic radii and systematic studies of interatomic distances in halides and chalcogenides. *Acta Crystallogr., Sect. A: Cryst. Phys., Diffraction, Theor. Gen. Crystallogr.* **1976**, *32*, 751–767.
- (21) Dorenbos, P. Determining binding energies of valence-band electrons in insulators and semiconductors via lanthanide spectroscopy. *Phys. Rev. B: Condens. Matter Mater. Phys.* **2013**, *87*, 035118.
- (22) Fan, L.; Lin, D.; Zhang, X.; Shi, Y.; Zhang, J.; Xie, J.; Lei, F.; Zhang, L. Local structures of Lu atoms in a core-shell approach for synthesis of Lu₂SiO₅ phase. *Chem. Phys. Lett.* **2016**, *644*, 41–44.
- (23) Ning, L.; Zhou, C.; Chen, W.; Huang, Y.; Duan, C.; Dorenbos, P.; Tao, Y.; Liang, H. Electronic properties of Ce³⁺-doped Sr₃Al₂O₅Cl₂: a combined spectroscopic and theoretical study. *J. Phys. Chem. C* **2015**, *119*, 6785–6792.
- (24) Tanner, P. A.; Fu, L.; Ning, L.; Cheng, B.-M.; Brik, M. G. Soft synthesis and vacuum ultraviolet spectra of YAG:Ce³⁺ nanocrystals: reassignment of Ce³⁺ energy levels. *J. Phys.: Condens. Matter* **2007**, *19*, 216213.
- (25) Jiao, H.; Wang, Y. Ca₂Al₂SiO₇:Ce³⁺,Tb³⁺: a white-light phosphor suitable for white-light-emitting diodes. *J. Electrochem. Soc.* **2009**, *156*, J117–J120.
- (26) Van der Kolk, E.; Dorenbos, P.; Vink, A.; Perego, R.; Van Eijk, C.; Lakshmanan, A. Vacuum ultraviolet excitation and emission properties of Pr³⁺ and Ce³⁺ in MSO₄ (M= Ba, Sr, and Ca) and predicting quantum splitting by Pr³⁺ in oxides and fluorides. *Phys. Rev. B: Condens. Matter Mater. Phys.* **2001**, *64*, 195129.
- (27) Dorenbos, P.; Pierron, L.; Dinca, L.; Van Eijk, C.; Kahn-Harari, A.; Viana, B. 4f–5d spectroscopy of Ce³⁺ in CaBPO₅, LiCaPO₄ and Li₂CaSiO₄. *J. Phys.: Condens. Matter* **2003**, *15*, 511.
- (28) Shi, R.; Xu, J.; Liu, G.; Zhang, X.; Zhou, W.; Pan, F.; Huang, Y.; Tao, Y.; Liang, H. Spectroscopy and Luminescence Dynamics of Ce³⁺ and Sm³⁺ in LiYSiO₄. *J. Phys. Chem. C* **2016**, *120*, 4529–4537.
- (29) Weber, M. Optical spectra of Ce³⁺ and Ce³⁺-sensitized fluorescence in YAlO₃. *J. Appl. Phys.* **1973**, *44*, 3205–3208.
- (30) Kodama, N.; Yamaga, M.; Kurahashi, T. Crystal field splitting and symmetry of Ce³⁺ polyhedra in oxide crystals. *Radiat. Eff. Defects Solids* **1999**, *151*, 159–164.
- (31) Dorenbos, P. The 5d level positions of the trivalent lanthanides in inorganic compounds. *J. Lumin.* **2000**, *91*, 155–176.
- (32) Dorenbos, P. Modeling the chemical shift of lanthanide 4 f electron binding energies. *Phys. Rev. B: Condens. Matter Mater. Phys.* **2012**, *85*, 165107.
- (33) Dorenbos, P. A review on how lanthanide impurity levels change with chemistry and structure of inorganic compounds. *ECS J. Solid State Sci. Technol.* **2013**, *2*, R3001–R3011.
- (34) Dorenbos, P. Ce³⁺ 5d-centroid shift and vacuum referred 4f-electron binding energies of all lanthanide impurities in 150 different compounds. *J. Lumin.* **2013**, *135*, 93–104.
- (35) Huang, B.; Sun, M. Energy conversion modeling of the intrinsic persistent luminescence of solids via energy transfer paths between transition levels. *Phys. Chem. Chem. Phys.* **2017**, *19*, 9457–9469.
- (36) Huang, B. Native point defects in CaS: Focus on intrinsic defects and rare earth ion dopant levels for up-converted persistent luminescence. *Inorg. Chem.* **2015**, *54*, 11423–11440.
- (37) Peng, Q.; Liu, C.; Hou, D.; Zhou, W.; Ma, C.-G.; Liu, G.; Brik, M. G.; Tao, Y.; Liang, H. Luminescence of Ce³⁺-Doped MB₂Si₂O₈ (M= Sr, Ba): A Deeper Insight into the Effects of Electronic Structure and Stokes Shift. *J. Phys. Chem. C* **2016**, *120*, 569–580.
- (38) Duan, C.-K.; Reid, M. F. Local field effects on the radiative lifetimes of Ce³⁺ in different hosts. *Curr. Appl. Phys.* **2006**, *6*, 348–350.
- (39) Zych, A.; de Lange, M.; de Mello Donegá, C.; Meijerink, A. Analysis of the radiative lifetime of Pr³⁺ d_f emission. *J. Appl. Phys.* **2012**, *112*, 013536.
- (40) Korotkov, A.; Atuchin, V. Accurate prediction of refractive index of inorganic oxides by chemical formula. *J. Phys. Chem. Solids* **2010**, *71*, 958–964.
- (41) Ueda, J.; Yagi, M.; Tanabe, S. Investigation of Luminescence and Photoacoustic Properties in Ce³⁺-Doped Ln₃Al₅O₁₂ (Ln = Lu, Y, Gd) Garnet. *ECS J. Solid State Sci. Technol.* **2016**, *5*, R219–R222.
- (42) Ueda, J.; Tanabe, S.; Nakanishi, T. Analysis of Ce³⁺ luminescence quenching in solid solutions between Y₃Al₅O₁₂ and Y₃Ga₅O₁₂ by temperature dependence of photoconductivity measurement. *J. Appl. Phys.* **2011**, *110*, 053102.
- (43) Ueda, J.; Dorenbos, P.; Bos, A. J.; Meijerink, A.; Tanabe, S. Insight into the thermal quenching mechanism for Y₃Al₅O₁₂:Ce³⁺ through thermoluminescence excitation spectroscopy. *J. Phys. Chem. C* **2015**, *119*, 25003–25008.

- (44) Yen, W.; Raukas, M.; Basun, S.; Van Schaik, W.; Happek, U. Optical and photoconductive properties of cerium-doped crystalline solids. *J. Lumin.* **1996**, *69*, 287–294.
- (45) Van der Kolk, E.; Dorenbos, P.; De Haas, J.; Van Eijk, C. Thermally stimulated electron delocalization and luminescence quenching of Ce impurities in GdAlO₃. *Phys. Rev. B: Condens. Matter Mater. Phys.* **2005**, *71*, 045121.
- (46) Jiao, H. Y.; Wang, Y. A potential red-emitting phosphor CaSrAl₂SiO₇:Eu³⁺ for near-ultraviolet light-emitting diodes. *Phys. B* **2012**, *407*, 2729–2733.
- (47) Blasse, G. The ultraviolet absorption bands of Bi³⁺ and Eu³⁺ in oxides. *J. Solid State Chem.* **1972**, *4*, 52–54.
- (48) Dorenbos, P. The Eu³⁺ charge transfer energy and the relation with the band gap of compounds. *J. Lumin.* **2005**, *111*, 89–104.
- (49) Luo, H.; Ning, L.; Dong, Y.; Bos, A. J.; Dorenbos, P. Electronic Structure and Site Occupancy of Lanthanide-Doped (Sr,Ca)₃(Y,Lu)-₂Ge₃O₁₂ Garnets: A Spectroscopic and First-Principles Study. *J. Phys. Chem. C* **2016**, *120*, 28743–28752.
- (50) Dorenbos, P. Charge transfer bands in optical materials and related defect level location. *Opt. Mater.* **2017**, *69*, 8–22.